Journal of Magnetism and Magnetic Materials 587 (2023) 171262

Contents lists available at ScienceDirect

Journal of Magnetism and Magnetic Materials

journal homepage: www.elsevier.com/locate/jmmm

Research article

Structure refinement and magnetic properties of synthetic $Co_3Ge_2O_5(OH)_4$ phyllogermanate

N.A. Belskaya [a,*], E.K. Khrapova [a], A.A. Ivanova [a], E.V. Eremin [b,c], S.I. Pavlov [a], A.A. Krasilin [a]

[a] Ioffe Institute, Polytechnicheskaya street, 26, St.-Petersburg, 194021, Russia
[b] Kirensky Institute of Physics, Akademgorodok 50, bld. 38, Krasnoyarsk, 660036, Russia
[c] Reshetnev Siberian State University of Science and Technology, 31, Krasnoyarsky Rabochy Av., Krasnoyarsk, 660037, Russia

ARTICLE INFO

Keywords:
Layered material
Lizardite structure
Hydrothermal synthesis
Crystal structure
Rietveld method
Antiferromagnetism/Ferromagnetism

ABSTRACT

$Co_3Ge_2O_5(OH)_4$ relates to a specific group of 1:1 layered compounds with an ability to form either platy or tubular particles depending on chemical composition. Despite successful synthesis and perspective application, there is a lack of information on its crystal structure and magnetic properties, granted by Co ions. $Co_3Ge_2O_5(OH)_4$ phyllogermanate nanoparticles have been obtained using a hydrothermal method and characterised using powder X-ray diffraction and magnetisation measurements. Triclinic symmetry with a 1:P1 space group has been established. The unit cell contains three layers perpendicular to the c crystallographic direction, with 7.6 Å spacing and $-b/3$ shift of the middle layer. At a low magnetic field of 100 Oe the compound undergoes a magnetic transition at $T_N = 5.2$ K. The field of 9 T is not sufficient to take the sample to a magnetically saturated state with an asymptotic magnetic moment of 2.43 μ_B/Co^{2+}. The estimations of the intralayer and interlayer exchange constants give values of $J_1/k_B = 2.75$ K and $J_2/k_B = 0.25$ K, respectively.

1. Introduction

Among the variety of serpentine group minerals, phyllosilicates (or layered silicates) with the general stoichiometric formula $Mg_3Si_2O_5(OH)_4$ holds a prominent place. Despite differences in composition (presence of impurity ions) and morphology [1,2], the 1:1 phyllosilicate structure conjoins two sheets: a metal-oxygen brucite-like octahedral sheet and a silicon–oxygen tetrahedral sheet [3–5]. The size mismatch between the sheets – the octahedral sheet is larger than the tetrahedral one – leads to bending of the layer and formation of phyllosilicate nanoscrolls with chrysotile structure. On the contrary, stabilisation of platy morphology, typical for lizardite, is usually caused by the presence of impurities like iron and aluminium [6–8].

$Me_3Ge_2O_5(OH)_4$ phyllogermanates (Me — metal ion) are synthetic analogues of natural magnesium phyllosilicates. So far, the synthesis of magnesium, nickel and cobalt phyllogermanates by a hydrothermal method from different precursors has been reported [9–15]. Their crystal structure was assumed to be similar to lizardite, however, in-deep studies were not carried out. Magnesium and nickel phyllogermanates form platy particles, although the calculated size mismatch value is larger than that for the similar phyllosilicates [16]. In contrast to platy lizardite-like $Me_3Ge_2O_5(OH)_4$, the existing $Al_2GeO_3(OH)_4$ phyllogermanates with imogolite structure [17] form predominantly double-walled nanotubes [18,19] due to the relatively large size mismatch [16].

Substitution of silicon by germanium ions significantly increases the size of the tetrahedral sheets (the ionic radius of Si^{4+} is 26 pm compared to 39 pm for Ge^{4+} [20]) and would switch the direction of lizardite layer bending (so the layer should scroll in a way analogical to halloysite [21,22]). However, arising competition between the strain and the surface energies of the layer for the direction of scrolling creates substantial hindrance for the synthesis of nanotubular phyllosilicates with halloysite structure [23], as well as for phyllogermanate analogues of lizardite. Despite the fact that phyllogermanate structure and formation mechanisms are still poorly understood, they have found application in catalysis, energy, and adsorption [10,11,24,25] fields due to the unique structure and wide possibilities of composition tuning (and, perhaps, morphology in the future).

Doping phyllosilicate and phyllogermanate with a transition metal ions opens a path for magnetic properties control. In this work we have synthesised and studied the crystal structure and magnetic properties of $Co_3Ge_2O_5(OH)_4$ phyllogermanate. As a result, the crystal structure has been refined, and magnetic subsystem parameters have been determined.

* Correspondence to: Laboratory of new inorganic materials, Ioffe Institute, Polytechnicheskaya St., 26, Saint-Petersburg 194021, Russia.
E-mail address: nbelsk@mail.ioffe.ru (N.A. Belskaya).

https://doi.org/10.1016/j.jmmm.2023.171262
Received 27 July 2023; Received in revised form 2 September 2023; Accepted 13 September 2023
Available online 17 September 2023

Table 1
Unit cell models used for refinement.

Model	Initial unit cell	Quantity of layers	Shift	Space group	R_{wp}, %
A	Lizardite 1T [3]	1	–	trigonal 157:P31 m	8.5
B	Serpentine [26]	1	–	triclinic 1:P1	7.9
C	Serpentine [26]	2	–	triclinic 1:P1	9.9
D	Lizardite 2H1 [3]	2	–	hexagonal 185:P63 cm	10.8
E	Serpentine [26]	2	layer 2 $-b/3$	triclinic 1:P1	8.5
F	Chrysotile [27]	2	–	monoclinic 9:C1c1	13.3
G	Serpentine [26]	3	layer 1 $-b/3$	triclinic 1:P1	10.5
H/Hm*	Serpentine [26]	3	layer 2 $-b/3$	triclinic 1:P1	7.2/4.6*
I	Serpentine [26]	3	layer 2 $-b/3$, layer 3 $-2b/3$	triclinic 1:P1	8.7
J	Serpentine [26]	6	layers 2 and 4 $-b/3$	triclinic 1:P1	12.6

* After atomic coordinates refinement.

2. Materials and methods

2.1. Synthesis of phyllogermanate

The preparation of $Co_3Ge_2O_5(OH)_4$ phyllogermanate was carried out by the reverse coprecipitation method similar to that described in [28]. For this purpose, a 0.06 L of 1M NaOH aqueous solution was prepared, then 2 g of GeO_2 was added and stirred for 1 h until complete dissolution of the oxide. Then 0.05 L of 0.5 M $CoCl_2 \cdot 6H_2O$ aqueous solution was added dropwise based on the molar ratio Co/Ge = 1.5, under constant stirring and argon flow to prevent oxidation of Co^{2+} to Co^{3+}. The resulting suspension was washed with distilled water by centrifugation to remove impurity chloride ions. The degree of washing was checked by qualitative reaction with $AgNO_3$. The precipitate was dried at 80 °C in air, ground in an agate mortar and placed in a 0.025 L PTFE-lined autoclave. Around 20 ml of distilled water was used as the hydrothermal medium. The hydrothermal treatment was carried out for 72 h at a temperature of 200 °C and a design pressure of 2 MPa. After the hydrothermal treatment, the product was dried at 80 °C in air.

2.2. Powder X-ray diffraction (PXRD)

2.2.1. The experiment

The sample was studied by powder X-ray diffraction (PXRD) using a Rigaku SmartLab 3 (Japan) with a cobalt cathode (λ = 1.789 Å) with a K_β-filter (Fe-foil) in Bragg–Brentano geometry by the angle $\theta - 2\theta$ in the range 5-120° with a step of 0.01° and a speed of 0.1 °/min. The cathode filament current was 35 mA and the accelerating voltage was 40 kV. The sample was mixed with silicon powder (NIST, USA) as a standard reference material to calibrate the position and shape of the reflections. Silicon was used as an internal standard for 2θ shift correction. The corrected reflections positions were then used as an external standard to correct the experimental pattern obtained without a silicon standard [27]. $SrTiO_3$ (CrysTec GmbH) was used as a standard to account for instrumental broadening.

2.2.2. Unit cell development

Due to the lack of information on the obtained compound in crystallographic databases, it was proposed that the structure of $Co_3Ge_2O_5(OH)_4$ is similar to that of magnesium phyllogermanate $Mg_3Ge_2O_5(OH)_4$. According to the work [26], magnesium phyllogermanate was characterised by polytypism with a complex sequence of $\pm b/3$ shifts of adjacent layers. Thus, the unit cell proposed in [26] consisted of 6 layers. This approach may better describe the unsystematic nature of layers stacking observed in lizardite [29]. Assuming $\pm b/3$ layer shifting a number $Co_3Ge_2O_5(OH)_4$ unit cell models were developed based on existing polytypes of lizardite 1T and 2H1 [3], chrysotile [27] and magnesium phyllogermanate 6T [26] (model ***J*** (Table 1)). Also, new one-, two-, three- and six-layer unit cell models have been developed using atomic coordinates and unit cell parameters. A description of each unit cell used for structure refinement is given in Table 1. Since it was possible to acceptably describe all the reflections using at least three-layer unit cell, unit cells with larger amount of layers were not considered except model ***J*** [26] for the purpose of comparison.

2.2.3. PXRD pattern treatment

Qualitative phase analysis was performed using Crystallography Open Database (COD) [30,31]. Unit cell parameters refinement was performed using the Rietveld method [32] in the Rigaku SmartLab Studio II software package. The B-spline function was used to describe the background, and the pseudo-Voigt function was used to fit the reflections. Axial shift was selected as the peak shift model. Crystallite shape was assumed to be anisotropic (ellipsoidal), and the eighth order spherical harmonics were chosen to account for texturing due to the multidirectional orientation. Average crystallite size and micro-strain were determined using the Halder–Wagner method [33]. The R_{wp}-factor for all unit cells is given in Table 1. Experimental and calculated PXRD patterns are shown in Figures. S1–S10. The unit cell with the smallest R_{wp}-factor (model ***H***) was used for crystal structure (atomic coordinates) refinement within 2% range of displacements allowed in each direction (model ***Hm***).

The valence states (r) of Co ions at different crystallographic positions of the models ***H*** and ***Hm*** were calculated by the bond valence sum method (BVS [34,35]):

$$r = \sum_{i=1}^{6} \exp\left(\frac{R_0 - R_i}{b_r}\right), \quad (1)$$

where $b_r = 0.37$, R_i is the Co – O interatomic distance, $R_0(Co^{2+})$=1.685; $R_0(Co^{3+})$=1.637 [35].

For each Co crystallographic position, an estimate of the octahedral distortion parameter was made using the equation:

$$\Delta = \frac{1}{6} \sum_{i=1}^{6} \left(\frac{R_i - \overline{R}}{\overline{R}}\right)^2, \quad (2)$$

where $\overline{R}$ is the average Co – O interatomic distance.

The distortion parameter of the coordination octahedron shows how much the octahedron is distorted relatively to the regular one (the larger the value of Δ is, the more distorted the octahedron is).

2.3. Electron microscopy

The elemental content of the obtained samples was studied by energy dispersive X-ray spectroscopy (EDS) using the X-ray Si(Li) microanalyser EDAX on a scanning electron microscope (SEM) FEI Quanta 200 (USA). The morphology of the sample was studied by scanning electron microscopy on a JEOL JSM 7001F (Japan).

2.4. Static magnetisation measurements

For magnetic measurements 4.9 mg of $Co_3Ge_2O_5(OH)_4$ powder was pressed into a tablet and filled with paraffin. The paraffin-filled tablet was placed in a sample holder using an optical microscope. DC magnetisation measurements were carried out using a commercial platform PPMS-9 (Quantum Design) in the temperature range 4.2–300 K and at the external fields up to 9 T. Temperature dependences of magnetisation were measured in field cooling (ZFC) and field heating

Table 2
Element content according to EDS.

Co, at.%	Ge, at.%	O, at.%	Co/Ge
26 ±3	18 ±1	56 ±3	1.4 ±0.2

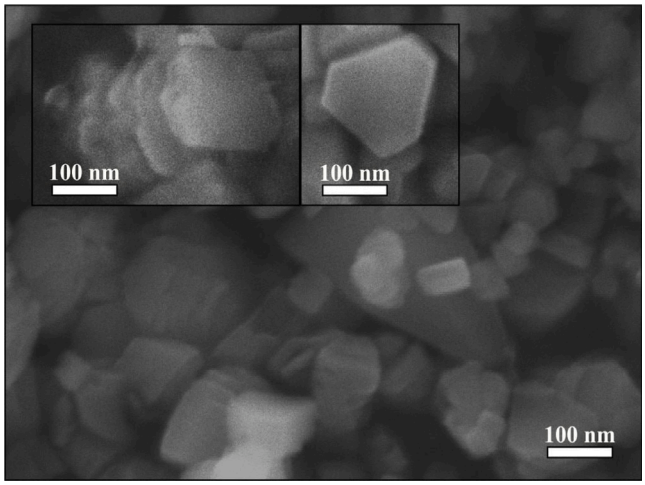

Fig. 1. SEM micrographs of $Co_3Ge_2O_5(OH)_4$ particles.

(FC) regimes. The magnetic data were corrected for the contribution of the sample holder to the magnetic susceptibility. Considering the random orientation of the particles with respect to the applied magnetic field, the measured magnetisation and susceptibility were taken as a random average.

3. Results and discussion

3.1. Particles composition and morphology

Fig. 1 shows SEM micrographs of $Co_3Ge_2O_5(OH)_4$ particles. Particles shape was close to hexagonal plates, that was consistent with observations of other phyllogermanates morphology [10,12,14,15]. The thickness of individual plates was about 50 nm, whereas the observed plate length remained in the 100–250 nm range. Particles tended to form pillar aggregates in the [001] direction. This aggregation trend may further promote formation of polytypes on the interface during the recrystallisation process via the oriented attachment [36].

The element content is given in Table 2. According to the analysed data, the sample was free from any impurities within detection limits, and the Co/Ge=1.5 molar ratio set by synthesis was maintained within the error limits.

3.2. Crystal structure

Fig. 2 demonstrates experimental and calculated (for the model ***H***) PXRD patterns of the sample. The pattern contained K_β radiation accompanying the most intense reflections because of low scanning speed. Negative COD database search for impurity phases like GeO_2 or CoOOH together with the EDS results approved single phase nature of the sample. In this context, all the observed diffraction peaks were attributed to the cobalt phyllogermanate phase.

Table 3 summarises the unit cell parameters, average crystallite size and micro-strain for the $Co_3Ge_2O_5(OH)_4$ sample. In comparison with single layer unit cells (models ***A*** and ***B***, Fig. S1–S2), the model ***H*** allowed us to describe an overwhelming number of low intensity reflections (see Fig. S8) indicating polytype formation.

Low micro-strain in the structure could originate from layer shifting in the unit cell or the possible presence of lattice defects. The crystallite

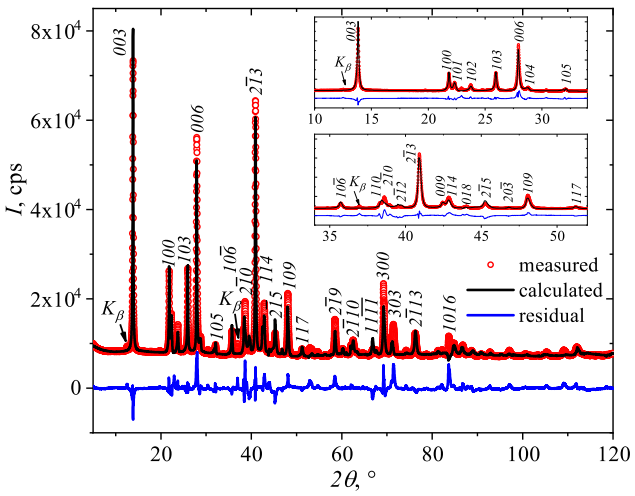

Fig. 2. Experimental, calculated, and residual PXRD patterns of $Co_3Ge_2O_5(OH)_4$. The theoretical pattern was calculated using the model ***H***. Arrows indicate the reflections caused by K_β radiation. The Miller indices are labelled above the reflections. Insets show magnified ranges of the PXRD pattern.

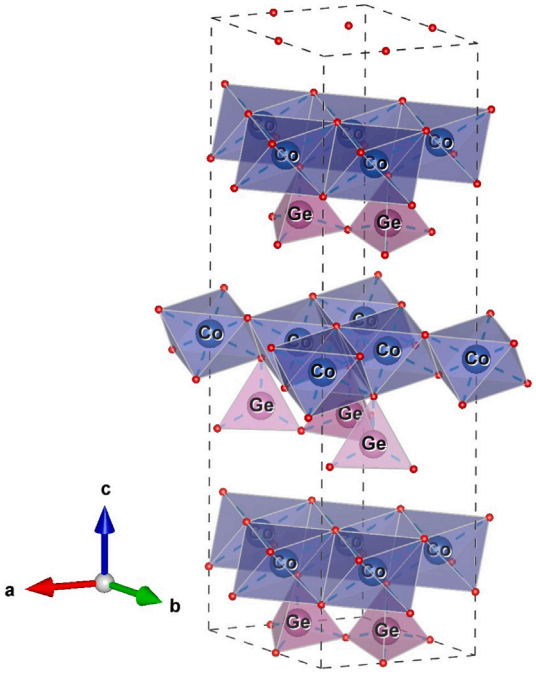

Fig. 3. Visualisation of $Co_3Ge_2O_5(OH)_4$ unit cell (model ***H***).

size averaged over all crystallographic directions was in the 45–50 nm (Table 3) range regardless of the unit cell used.

The image of the unit cell (model ***H***, Table 1) is shown in Fig. 3. Although this unit cell belongs to the triclinic syngony (which is characterised by the inequality of all unit cell parameters), its parameters are close to the hexagonal syngony inherent in minerals with the structure of lizardite. The unit cell included three layers that extended perpendicular to the c crystallographic direction with 7.6 Å spacing (around 4.3 Å was for the layer thickness, and around 3.3 Å was for the distance between the layers). In addition, the middle layer was shifted relatively to its neighbours by $-b/3$. It might be possible that the layers shifting occurs rather randomly like it was observed for the lizardite sample [29], and the unit cell proposed reflected some averaged case, an existence of "ordered" (no shifting) and "disordered"

Table 3
Unit cell parameters, crystallite size and micro-strain for the models *H* and *Hm*.

Parameter	Model *H*	Model *Hm*
a, Å	5.4571(2)	5.4566(2)
b, Å	5.4467(6)	5.4463(3)
c, Å	22.2432(9)	22.2437(6)
α, °	90.220(8)	90.133(5)
β, °	89.995(2)	89.997(2)
γ, °	120.090(4)	120.060(4)
V, Å^3	572.04(6)	572.13(6)
Crystallite size, Å	482(2)	482(2)
Micro-strain, %	0.116(2)	0.116(2)

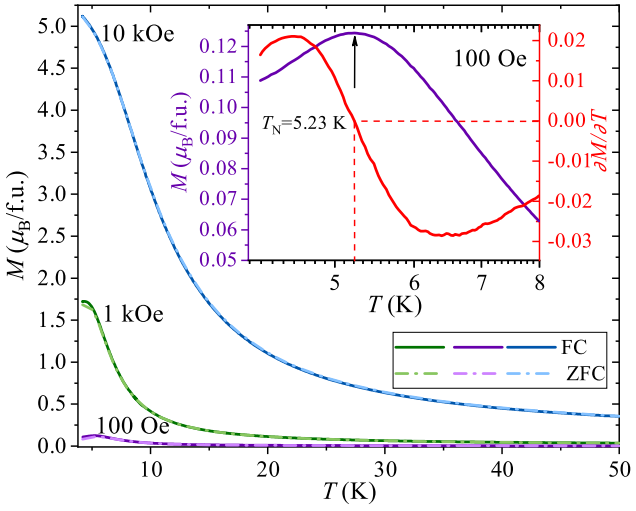

Fig. 4. Temperature dependence of the magnetisation measured at 100 Oe, 1 kOe, 10 kOe fields on a powder sample, the inset in the figure shows the dependence of $M(T)$ (FC) in an enlarged scale H = 100 Oe (violet curve) and first derivative of magnetisation (red curve) .

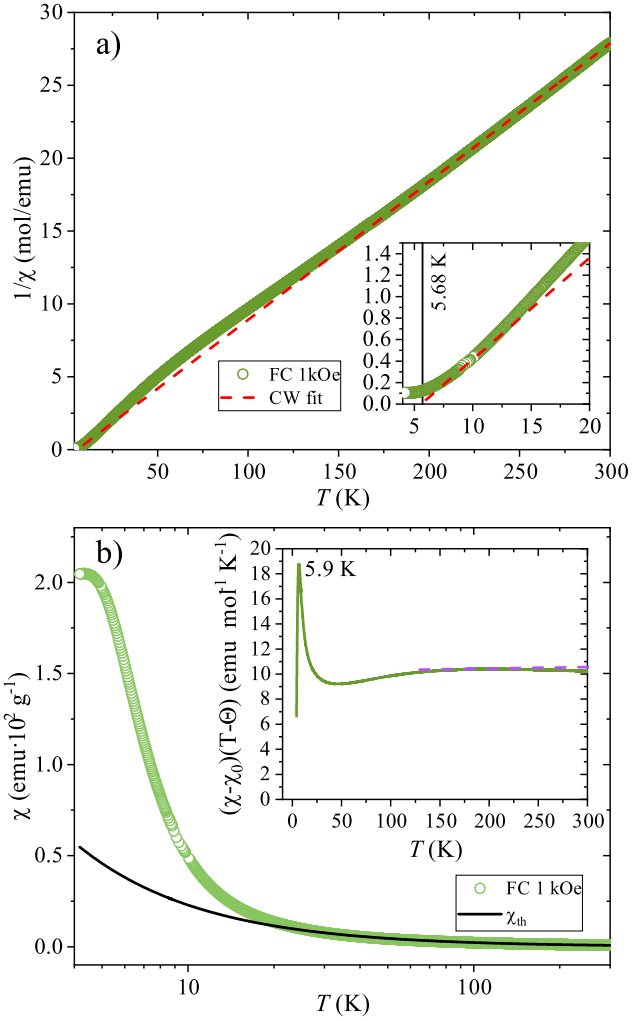

Fig. 5. a) Temperature dependence of the reduced magnetic susceptibility in a 1 kOe field (green symbol) and the result of fitting by the linear Curie–Weiss law (dashed red curve). The inset shows the intersection of the Curie–Weiss law approximation with the abscess axis. b) Temperature dependence of the magnetic susceptibility in the 1 kOe field (green symbol), and result the fit using Eq. (4) (black solid curve) on a logarithmic scale. The inset shows the temperature dependence of the reduced magnetic susceptibility $(\chi - \chi_0)(T - \theta)$, the horizontal dashed line corresponds to the Curie–Weiss law at high temperature.

(presence of shifting) types of interfaces in a certain proportion in the layered structure.

After atomic coordinates refinement (model ***Hm***, see Fig. S11), the unit cell parameters remained almost unchanged compared to the model ***H*** (Tables S1–S3). The R_{wp} factor value was reduced from 7.2 to 4.6%, however, some Co-containing polyhedra acquired notable distortion (Tables 1, S2,S3). The most distorted crystallographic positions (see Eq. (2)) for the refined structure belong to the middle (M4,M6) and upper (M8) layers. On average, the Δ value increased by 2–3 orders of magnitude after the atomic coordinates refinement (Table S4). The tendency of polyhedra distortion was characteristic for related phyllosilicates with chrysotile [27,37] and halloysite [38] structure. Calculations via the BVS method (see Eq. (1)) yielded Co^{2+} state for each Co position both before and after atomic coordinates refinement (Table S4).

The CIF files of unit cell models ***H*** and ***Hm*** are available at the end of Supplementary Material.

3.3. Magnetic behaviour

The temperature dependences of the magnetisation of $Co_3Ge_2O_5(OH)_4$ are displayed in Fig. 4. No peculiarities are observed down to low temperatures. The intensive rise in the magnetisation below 40 K indicates the growing ferromagnetic moment. Nevertheless, at low magnetic field (100 Oe) a clear maximum at T_N = 5.2 K is observed with noticeable divergence of FC and ZFC curves. Below critical temperature ZFC curve rapidly decreases assuming the antiferromagnetic correlations are developed. For more accurate determination of the Néel temperature, we used the first derivative of the magnetisation (inset in Fig. 4), the minimum of which corresponds to the value of 5.23 K. This anomaly can be attributed to the interlayer antiferromagnetic coupling similarly to those found for the β-$Co(OH)_2$ [39] and $Co_2(NO_3)(OH)_3$ [40] at 10 and 9.8 K (Table 4), respectively. The anomaly is suppressed by the magnetic field reflecting the antiferromagnetic interactions are rather weak. At the high magnetic fields the magnetic anomaly is gradually smoothed. The splitting between the FC and ZFC curves could have several reasons. It is often observed in spin glasses or in superparamagnetic systems. It could also be due to blocking of domain wall motion at low temperatures [41,42] or be the result of some nanoparticle size effects, since the thickness of the plates can be roughly estimated to be around 40 nm. A similar effect was observed in α-$Ni(OH)_2$ [43], β-$Ni(OH)_2$ [43] and β-$Co(OH)_2$ [39, 40,44] nanoparticles, whose structure is close to octahedral sheets of $Co_3Ge_2O_5(OH)_4$.

Fig. 5a shows the temperature dependence of the inverse magnetic susceptibility treated by the linear Curie–Weiss law. The fitting range was 200–300 K. The red dashed line indicates the intersection of the fitting with the abscess axis. The fit parameters are obtained values, θ = 5.68 ± 0.04 K, C = 10.56 ± 0.03 emu/mol. The positive value

Table 4
Interlayer spacing (d) and magnetic parameters of $Co_3Ge_2O_5(OH)_4$ phyllogermanate and related layered compounds.

Compound (ref.)	d, Å	T_C, K	T_N, K	θ, K	μ_{eff}^{exp}, μ_B/Me^{2+}	η	J_1/k_B, K	J_2/k_B, K	M_s, μ_B/Me^{2+}
α-$Ni(OH)_2$ [43]	8.6	16	–	35	3.13	2.1875	4.38	0.14	1.08
β-$Ni(OH)_2$ [46]	4.6	–	26.5	20.5	2.92	0.7736	3.25	−0.32	1.16
$Ni_3Si_2O_5(OH)_4$ [42]	7.3	23.7	–	38	3.48	1.6034	–	–	1.97
α-$Co(OH)_2$ [39]	8.7	108	–	118	–	1.0926	–	–	–
β-$Co(OH)_2$ [39]	4.8	–	10.4	10.3	–	0.9981	–	–	–
β-$Co(OH)_2$ [44]	4.7	–	9.2	9.5	5.19	1.0326	1.67	−0.17	2.59
β-$Co(OH)_2$ [40]	7.0	8.4	–	–	–	–	2.1	−2.57	2.90
$Co_2(NO_3)(OH)_3$ [40]	7.0	–	6.7	–	–	–	7.4	−0.23	2.80
$Co_3Ge_2O_5(OH)_4$ (present study)	7.6	–	5.2	6.1	5.23	1.1731	2.75	0.25*	2.43

* Not including the sign of exchange.

of the paramagnetic Curie temperature indicates the dominance of ferromagnetic interactions, as can be seen in the figure inset. However, such a narrow fitting range is not sufficient for accurate determination of magnetic parameters.

In the larger temperature range , the magnetic susceptibility χ obeys the modified Curie–Weiss law (inset in Fig. 5b) [45]:

$$\chi(T) = \chi_0 + C/(T-\theta), \tag{3}$$

The fit parameters are returned parameter values $\chi_0 = (4.18 \pm 0.02) \cdot 10^{-3}$ emu/mol, $\theta = 6.09 \pm 0.03$ K, $C = 10.27 \pm 0.01$ emu/mol. The temperature independent term $\chi_0 = \chi_{dia} + \chi_{vV}$ includes the diamagnetic contribution χ_{dia} associated with the internal electron shells and the paramagnetic van Vleck contribution χ_{vV} associated with the contribution from quantum transitions between the ground and excited states of ions with partially filled electron shells. The diamagnetic contribution, determined by the sum of the Pascal constants [47], was found to be $\chi_{dia} = -1.58 \cdot 10^{-4}$ emu/mol.

The inset in Fig. 5b displays the temperature dependence of the value of $(\chi - \chi_0)(T-\theta)$ vs temperature. The dashed straight line presents the Curie–Weiss law. When the temperature was lowered to 140 K, the experimental curve deviated downward from the horizontal line. This could indicate a slight increase in near-order antiferromagnetic correlations. However, below 50 K, the dependence increased sharply and attained a maximum at 5.9 K. Although a monotonic growth of $M(T)$ is observed in the 1 kOe field, there is a slight hint of the presence of antiferromagnetic correlations in the inset in Fig. 5b. The impression is that, like β-$Co(OH)_2$ [39,44] in $Co_3Ge_2O_5(OH)_4$, the ferromagnetic planes are linked by antiferromagnetic exchange. The calculated effective magnetic moment of around 5.23 μ_B/Co^{2+} is slightly larger than the spin-only one 3.87 μ_B for Co^{2+} ion and is in good agreement with the values reported for divalent cobalt in octahedral environment (4.7–5.2 μ_B [45,48]). Using the experimental value of the magnetic moment μ_{eff}, we can estimate the g-factor. The square of the effective magnetic moment is 27.35 μ_B^2, so the g-factor value was 2.7. The obtained g-factor value was typical for Co^{2+} [45] ions, and it indicated substantial contribution of orbital momentum to the effective magnetic moment.

The positive value of the Curie–Weiss temperature θ indicates the predominance of the ferromagnetic spin correlations. In general, the θ is the sum of the parameters of all exchange magnetic interactions in the system. This value decreases in the row α-$Co(OH)_2$, β-$Co(OH)_2$ [39], β-$Co(OH)_2$ [44]. β-$Co(OH)_2$, $Co_2(NO_3)(OH)_3$ [40], and $Co_3Ge_2O_5(OH)_4$ (Table 4) reflecting the decrease in the energy of magnetic exchange interactions and being in accordance with the decrease in the magnetic ordering temperature. This can be attributed to a decrease in the distances between cobalt layers $[CoO_6]_\infty$ (see Table 4).

It is interesting to compare the observed magnetic behaviour of $Co_3Ge_2O_5(OH)_4$ with related compounds like $Ni(OH)_2$ and $Co(OH)_2$. Considering β-$Co(OH)_2$ [39,44], θ value was found to be positive (see Table 4). However, magnetic ordering inside the hexagonal β-$Co(OH)_2$ layer was ferromagnetic with spins lying perpendicular to c axis, while in the adjacent layer the spins were antiferromagnetically ordered with respect to the former. Transition to forced ferromagnetic state with all spins aligned towards the applied field occurred at $H > H_{C2}$ (32 kOe). Similar behaviour was observed for β-$Ni(OH)_2$ [46] with H_{C2} value being 55 kOe. Next, both hydroxides possess an α-modification, in which interlayer distance is almost twice as large (Table 4). Increased c parameter in both cases resulted in ferromagnetic behaviour [39,43]. We assume, by analogy, that in $Co_3Ge_2O_5(OH)_4$ the ferromagnetic component in the exchange interactions belonged to Co^{2+} interaction within the octahedral sheet, while the weak antiferromagnetic correlations were inherent to the interlayer interactions. An increased distance between adjacent octahedral sheets (because of additional GeO_4 sheet, see Fig. 3) weakened interlayer interactions. This feature also relieved from the necessity of applying large fields (greater than the H_{C2} values) in order to reach ferromagnetic transition.

Additional details on the type of magnetic ordering can be obtained from analysis of exchange coupling constants. Fig. 5b shows an analysis of the high-temperature part of the magnetic susceptibility using a fit by high temperature series (HTS) for $S = 3/2$ and 2D Ising triangular lattice valid for $Co_3Ge_2O_5(OH)_4$ [43]

$$\chi = \frac{2N_A g^2 \mu_B^2}{3M_{mol} k_B T} \sum_{n=0}^{11} a_n \left(\frac{2J_1}{k_B T}\right)^n, \tag{4}$$

where M_{mol} is the molar mass of the sample, g is the Lande factor ($g = 2.7$ obtained by CW fit), N_A is Avogadro number, k_B — Boltzmann constant, μ_B — bohr magneton, J_1 — exchange constant of in-plane (intralayer) coupling, $a_0 = 3$, $a_1 = 7.5$, $a_2 = 14.5$, $a_3 = 24.375$, $a_4 = 39.8625$, $a_5 = 66.6875$, $a_6 = 110.759$, $a_7 = 175.0923$, $a_8 = 262.69675$, $a_9 = 386.2849$, $a_{10} = 574.443$, $a_{11} = 861.4927$ [49]. A 2D Ising model valid $S = 1/2$ is used to fit magnetic susceptibility. It should be mentioned, and that the same equation is being used for $S = 3/2$. The fitting parameter here was J_1. The fit curve (Fig. 5*b*) is agreed well with an experimental one in wide T-interval, showing deviation at below 20 K. Fitting gives $J_1/k_B = 2.75$ K (see Table 4). The Eq. (4) included only the dominant intralayer exchange coupling constant J_1. Using $T_N = 5.2$ K, the interlayer exchange coupling constants J_2 was estimated using the relation [43,50]:

$$T_C = \frac{4\pi|J_1|}{\ln(|J_1|/|J_2|)}. \tag{5}$$

The estimation in with way yields the value of $J_2/k_B = 0.25$ K (Table 4). At the same time, Eq. (5) does not take into account the sign of the exchange, only the magnitude.

A propensity for the long-range magnetic ordering was estimated using the parameter of magnetic frustration:

$$\eta = |\theta|/T_{C,N}. \tag{6}$$

Strong magnetic frustrations ($\eta > 5$) interfere with long-range order and may hold disordered (spin glass) state of the system at low temperatures. Low paramagnetic Curie temperature $\theta = 6.1 \pm 0.03$ K and

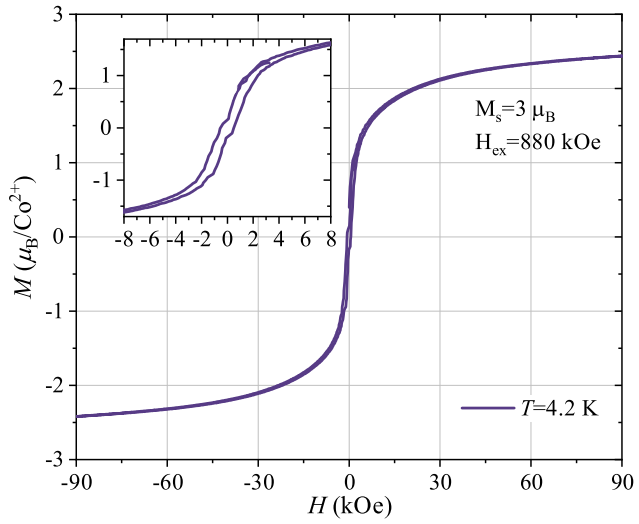

Fig. 6. Dependence of magnetisation M on magnetic field H measured in the 4.2 K. The upper inset shows the hysteresis loops in an enlarged scale.

T_N = 5.2 K yielded $\eta = 1.17 \pm 0.07$ (Table 4), which spoke in favour of the absence of magnetic frustrations in $Co_3Ge_2O_5(OH)_4$. Therefore, we attributed relatively low T_N value (see Table 4) mainly to the presence of micro-strain (Table 3) and adjacent layer shifting (Fig. 3).

More information can be obtained from the isothermal magnetisation curves (Fig. 6). The shift of the hysteresis loop along the field axis (exchange bias) common in nanostructures, especially with ferromagnetic/antiferromagnetic interfaces [51]. The coercivity value was typical with to respect to related $Ni_3Si_2O_5(OH)_4$ phyllosilicate near the transition [42]. For comparison with other compounds, Fig. 6 shows the magnetisation isotherm at T = 4.2 K recalculated per cobalt ion. As can be seen from Table 4, the maximum saturation magnetisation for $Co_3Ge_2O_5(OH)_4$ is slightly lower than for other cobalt compounds with a layered structure. Measurements in the high fields (up to 9 T) show the magnetisation does not saturate at T = 4.2 K. The magnetic moment $M(H = 9T)$=2.43 μ_B/Co^{2+} is about 81% of $M_s = zgS\mu_B$. Using the linear part of $M(H)$ curve at high fields $\chi_{AFM} = 1.02325 \cdot 10^{-5}$ μ_B/(Oe) one can estimate the value of exchange field H_{ex} = 880 kOe. Thus, the $Co_3Ge_2O_5(OH)_4$ system is far from saturation at 90 kOe. The inset in Fig. 6 shows enlarged hysteresis loops, which clearly witnessed the ferromagnetic behaviour of $Co_3Ge_2O_5(OH)_4$. The rather narrow loops, which coercivity H of about 100 Oe suggest some domain structure in the ferromagnetically coupled spins in the $Co_3Ge_2O_5(OH)_4$ planes.

4. Conclusions

Successful hydrothermal synthesis of single-phase platy 1:1 cobalt phyllogermanate allowed us to carry out its structure refinement and DC magnetic measurements for the first time. The most probable quasi-hexagonal unit cells with R_{wp} factors 7.2 and 4.6% were developed on the basis of three lizardite-like layers with $-b/3$ shift of the middle layer. The achieved decrease of the R_{wp} factor was mainly because of distortion of Co-containing octahedra. The unit cell parameters were a = 5.4566(2) Å, b = 5.4463(3) Å, c = 22.2437(6) Å, α = 90.133(5)°, β = 89.997(2)°, and γ = 120.060(4)° for the refined unit cell. At T_N= 5.2 K and low magnetic fields the $Co_3Ge_2O_5(OH)_4$ undergoes magnetic transition probably due to antiferromagnetic coupling between adjacent $[CoO_6]_\infty$ layers. The application of high magnetic field overcomes this antiferromagnetic interlayer interaction resulting in the ferromagnetic-like behaviour. The estimation of the intralayer (J_1/k_B = 2.75 K) and interlayer (J_2/k_B = 0.25 K) exchange interactions is in accordance with the quasi 2D magnetic structure. The ferromagnetic order is established due to the enlarged interlayer distance in comparison with the related compound like β-$Co(OH)_2$, thus preventing a mutual influence on the intralayer spin arrangement.

CRediT authorship contribution statement

N.A. Belskaya: Conceptualization, Validation, Formal analysis, Investigation, Data curation, Writing – original draft, Visualization, Project administration, Funding acquisition. **E.K. Khrapova:** Formal analysis, Investigation, Resources, Data curation, Writing – original draft, Visualization. **A.A. Ivanova:** Investigation, Resources, Visualization. **E.V. Eremin:** Investigation, Resources. **S.I. Pavlov:** Investigation, Resources. **A.A. Krasilin:** Conceptualization, Supervision, Writing – review & editing.

Declaration of competing interest

The authors declare the following financial interests/personal relationships which may be considered as potential competing interests: Belskaya Nadejda reports financial support was provided by Russian Science Foundation. Khrapova Ekaterina reports financial support was provided by Russian Science Foundation.

Data availability

Data will be made available on request.

Acknowledgements

The authors are grateful to Dr. N.V. Kazak and Dr. A.A. Levin for a lot of fruitful discussions. Magnetisation measurements were carried out in the Common Access Facility Centres of SBRAS (Krasnoyarsk, Russia) X-ray powder diffraction measurements were performed at the Engineering Centre of St. Petersburg State Institute of Technology.

The study was supported by grant No. 23-22-00245 of the Russian Science Foundation, https://rscf.ru/project/23-22-00245/.

Appendix A. Supplementary data

Supplementary material related to this article can be found online at https://doi.org/10.1016/j.jmmm.2023.171262.

References

[1] N.J. Page, Chemical differences among the serpentine polymorphs, Am. Mineral. 53 (1–2) (1968) 201–215, URL https://pubs.geoscienceworld.org/msa/ammin/article-abstract/53/1-2/201/542380/Chemical-differences-among-the-serpentine.

[2] E.J.W. Whittaker, J. Zussman, The characterization of serpentine minerals by X-ray diffraction, Mineral. Mag. J. Mineral. Soc. 31 (233) (1956) 107–126, http://dx.doi.org/10.1180/minmag.1956.031.233.01.

[3] M. Mellini, V. Trommsdorff, R. Compagnoni, Antigorite polysomatism: Behaviour during progressive metamorphism, Contrib. Mineral. Petrol. 97 (2) (1987) 147–155, http://dx.doi.org/10.1007/BF00371235.

[4] E.N. Korytkova, A.V. Maslov, L.N. Pivovarova, I.A. Drozdova, V.V. Gusarov, Formation of $Mg_3Si_2O_5(OH)_4$ nanotubes under hydrothermal conditions, Glass Phys. Chem. 30 (1) (2004) 51–55, http://dx.doi.org/10.1023/B:GPAC.0000016397.29132.21.

[5] E.N. Korytkova, L.N. Pivovarova, Hydrothermal synthesis of nanotubes based on $(Mg,Fe,Co,Ni)_3Si_2O_5(OH)_4$ hydrosilicates, Glass Phys. Chem. 36 (1) (2010) 53–60, http://dx.doi.org/10.1134/S1087659610010104.

[6] A. Bloise, E. Belluso, E. Barrese, D. Miriello, C. Apollaro, Synthesis of Fe-doped chrysotile and characterization of the resulting chrysotile fibers, Cryst. Res. Technol. 44 (6) (2009) 590–596, http://dx.doi.org/10.1002/crat.200900135.

[7] E.N. Korytkova, L.N. Pivovarova, I.A. Drosdova, V.V. Gusarov, Hydrothermal synthesis of nanotubular Co-Mg hydrosilicates with the chrysotile structure, Russ. J. Gen. Chem. 77 (10) (2007) 1669–1676, http://dx.doi.org/10.1134/S1070363207100039.

[8] A.A. Krasilin, V.V. Gusarov, Control over morphology of magnesium-aluminum hydrosilicate nanoscrolls, Russ. J. Appl. Chem. 88 (12) (2015) 1928–1935, http://dx.doi.org/10.1134/S10704272150120046.

[9] D.M. Roy, R. Roy, An experimental study of the formation and properties of synthetic serpentines and related layer silicate minerals, Am. Mineral. 39 (11–12) (1954) 957–975, URL https://pubs.geoscienceworld.org/msa/ammin/article-abstract/39/11-12/957/539434/An-experimental-study-of-the-formation-and.

[10] N. Zhang, B. Yang, Y. He, Y. He, X. Liu, M. Liu, G. Song, G. Chen, A. Pan, S. Liang, R. Ma, S. Venkatesh, V.A.L. Roy, Serpentine Ni_3 Ge_2 O_5 $(OH)_4$ nanosheets with tailored layers and size for efficient oxygen evolution reactions, Small 14 (48) (2018) e1803015., http://dx.doi.org/10.1002/smll.201803015, arXiv:30328265.

[11] D. Luo, B. Yang, Z. Mei, Q. Kang, G. Chen, X. Liu, N. Zhang, Tuning the d-band states of Ni-based serpentine materials via Fe^{3+} doping for efficient oxygen evolution reaction, ACS Appl. Mater. Interfaces 14 (47) (2022) 52857–52867, http://dx.doi.org/10.1021/acsami.2c14720.

[12] A.A. Krasilin, E.K. Khrapova, Effect of hydrothermal treatment conditions on formation of nickel hydrogermanate with platy morphology, Russ. J. Appl. Chem. 90 (1) (2017) 22–27, http://dx.doi.org/10.1134/S1070427217010049.

[13] O. Yamaguchi, H. Matumoto, S. Morikawa, K. Shimizu, Preparation and thermal behavior of magnesium-germanium hydroxide, J. Am. Ceram. Soc. 66 (9) (1983) c169–c170, http://dx.doi.org/10.1111/j.1151-2916.1983.tb10631.x.

[14] B. Yang, N. Zhang, G. Chen, K. Liu, J. Yang, A. Pan, M. Liu, X. Liu, R. Ma, T. Qiu, Serpentine $Co_xNi_{3-x}Ge_2O_5(OH)_4$ nanosheets with tuned electronic energy bands for highly efficient oxygen evolution reaction in alkaline and neutral electrolytes, Appl. Catal. B 260 (2020) 118184, http://dx.doi.org/10.1016/j.apcatb.2019.118184.

[15] R. Perbost, M. Amouric, J. Olives, Influence of cation size on the curvature of serpentine minerals: HRTEM-AEM study and elastic theory, Clays Clay Miner. 51 (4) (2003) 430–438, http://dx.doi.org/10.1346/CCMN.2003.0510409.

[16] A.A. Krasilin, E.K. Khrapova, T.P. Maslennikova, Cation doping approach for nanotubular hydrosilicates curvature control and related applications, Crystals 10 (8) (2020) 654, http://dx.doi.org/10.3390/cryst10080654.

[17] I.S. Popov, A.N. Enyashin, Imogolite: Curvature-induced hospitality for trivalent dopants, Phys. Status Solidi b 258 (10) (2021) 2100188, http://dx.doi.org/10.1002/pssb.202100188.

[18] C. Levard, A. Thill, A. Avellan, C. Mauroy, V. Vidal, A.P.C. Campos, A. Masion, J. Rose, Alignment of Ge-imogolite nanotubes in isomalt with tunable inter-tube distances, RSC Adv. 7 (34) (2017) 21323–21327, http://dx.doi.org/10.1039/C7RA01380A.

[19] E. Paineau, S. Rouzière, G. Monet, C.C. Diogo, I. Morfin, P. Launois, Role of initial precursors on the liquid-crystalline phase behavior of synthetic aluminogermanate imogolite nanotubes, J. Colloid Interface Sci. 580 (2020) 275–285, http://dx.doi.org/10.1016/j.jcis.2020.07.036.

[20] R.D. Shannon, Revised effective ionic radii and systematic studies of interatomic distances in halides and chalcogenides, Acta Crystallogr. Sect. A: Cryst. Phys. Diff. Theor. General Crystallogr. 32 (5) (1976) 751–767.

[21] E. Joussein, S. Petit, J. Churchman, B. Theng, D. Righi, B. Delvaux, Halloysite clay minerals—a review, Clay Miner. 40 (4) (2005) 383–426.

[22] V.A. Drits, B.A. Sakharov, S. Hillier, Phase and structural features of tubular halloysite (7 Å), Clay Miner. 53 (4) (2018) 691–720, http://dx.doi.org/10.1180/clm.2018.57.

[23] A.A. Krasilin, Energy modeling of competition between tubular and platy morphologies of chrysotile and halloysite layers, Clays Clay Miner. 68 (5) (2020) 436–445, http://dx.doi.org/10.1007/s42860-020-00086-6.

[24] D. Luo, Y. Zang, Q. Kang, G. Chen, X. Liu, N. Zhang, Serpentine $Ni_3Ge_2O_5(OH)_4$ nanosheets grow on porous Mo_2N for an efficient oxygen evolution reaction, Energy Fuels 36 (19) (2022) 11467–11476, http://dx.doi.org/10.1021/acs.energyfuels.2c01025.

[25] N. Wen, K. Zhang, J. Feng, Z. Zhou, S. Chen, Y. Wang, S. Liu, Q. Kuang, Y. Dong, Y. Zhao, One-step in situ hydrothermal synthesis of layered $Ni_3Ge_2O_5(OH)_4$/carbon nanocomposite with superior sodium storage properties, J. Electroanal. Chem. 887 (2021) 115171, http://dx.doi.org/10.1016/j.jelechem.2021.115171.

[26] S.H. Hall, S. Guggenheim, P. Moore, S.W. Bailey, The structure of unst-type 6-layer serpentines, Can. Mineral. 14 (3) (1976) 314–321, URL https://pubs.geoscienceworld.org/canmin/article-abstract/14/3/314/11113/The-structure-of-unst-type-6-layer-serpentines.

[27] A. Levin, E. Khrapova, D. Kozlov, A. Krasilin, V. Gusarov, Structure refinement, microstrains and crystallite sizes of Mg-Ni-phyllosilicate nanoscroll powders, J. Appl. Crystallogr. 55 (3) (2022) 484–502, http://dx.doi.org/10.1107/S1600576722003594.

[28] E.K. Khrapova, D.A. Kozlov, A.A. Krasilin, Hydrothermal synthesis of hydrosilicate nanoscrolls $(Mg_{1-x}Co_x)_3Si_2O_5(OH)_4$ in a Na_2SO_3 solution, Russ. J. Inorg. Chem. 67 (6) (2022) 839–849, http://dx.doi.org/10.1134/S0036023622060110.

[29] I. Dódony, P.R. Buseck, Serpentines close-up and intimate: An HRTEM view, Int. Geol. Rev. 46 (6) (2004) 507–527, http://dx.doi.org/10.2747/0020-6814.46.6.507.

[30] S. Gražulis, D. Chateigner, R.T. Downs, A.F.T. Yokochi, M. Quirós, L. Lutterotti, E. Manakova, J. Butkus, P. Moeck, A. Le Bail, Crystallography open database – an open-access collection of crystal structures, J. Appl. Crystallogr. 42 (4) (2009) 726–729, http://dx.doi.org/10.1107/S0021889809016690.

[31] A. Vaitkus, A. Merkys, S. Gražulis, Validation of the crystallography open database using the crystallographic information framework, J. Appl. Crystallogr. 54 (2) (2021) 661–672, http://dx.doi.org/10.1107/S1600576720016532.

[32] H.M. Rietveld, Line profiles of neutron powder-diffraction peaks for structure refinement, Acta Crystallogr. 22 (1) (1967) 151–152, http://dx.doi.org/10.1107/S0365110X67000234.

[33] N.C. Halder, C.N.J. Wagner, Separation of particle size and lattice strain in integral breadth measurements, Acta Crystallogr. 20 (2) (1966) 312–313, http://dx.doi.org/10.1107/S0365110X66000628.

[34] F. Mohri, A new relation between bond valence and bond distance, Acta Crystallogr. Sect. B 56 (Pt) (2000) 4, http://dx.doi.org/10.1107/s0108768100005401, arXiv:10944253.

[35] I.D. Brown, D. Altermatt, Bond-valence parameters obtained from a systematic analysis of the inorganic crystal structure database, Acta Crystallogr. Sect. B 41 (4) (1985) 244–247, http://dx.doi.org/10.1107/S0108768185002063.

[36] V.K. Ivanov, A.Y. Baranchikov, P.P. Fedorov, V.V. Osiko, Oriented attachment of particles: 100 years of investigations of non-classical crystal growth, Russian Chem. Rev. (Print) 83 (12) (2014) 1204–1222, http://dx.doi.org/10.1070/RCR4453.

[37] G. Falini, E. Foresti, M. Gazzano, A.F. Gualtieri, M. Leoni, I.G. Lesci, N. Roveri, Tubular-shaped stoichiometric chrysotile nanocrystals, Chem – A Eur. J. 10 (12) (2004) 3043–3049, http://dx.doi.org/10.1002/chem.200305685.

[38] H.L. Zhang, X.R. Lei, C.J. Yan, H.Q. Wang, G.Q. Xiao, J.R. Hao, D. Wang, X.M. Qiu, Analysis on crystal structure of 7Å -halloysite, Adv. Mater. Res. 415–417 (2012) 2206–2214, http://dx.doi.org/10.4028/www.scientific.net/AMR.415-417.2206.

[39] A. Debnath, S. Bhattacharya, S.K. Saha, Observation of ferromagnetic ordering in a stable α–$Co(OH)_2$ phase grown on a MoS_2 surface, Phys. Rev. B 96 (21) (2017) 214433, http://dx.doi.org/10.1103/PhysRevB.96.214433.

[40] P. Rabu, S. Angelov, P. Legoll, M. Belaiche, M. Drillon, Ferromagnetism in triangular cobalt(II) layers: Comparison of cobalt dihydroxide and cobalt nitrate hydroxide $(Co_2(NO_3)(OH)_3)$, Inorg. Chem. 32 (11) (1993) 2463–2468, http://dx.doi.org/10.1021/ic00063a043.

[41] N.A. Chernova, Y. Song, P.Y. Zavalij, M.S. Whittingham, Solitary excitations and domain-wall movement in the two-dimensional canted antiferromagnet $(C_2N_2H_{10})_{1/2}FePO_4(OH)$, Phys. Rev. B 70 (14) (2004) 144405, http://dx.doi.org/10.1103/PhysRevB.70.144405.

[42] A.A. Krasilin, A.S. Semenova, D.G. Kellerman, V.N. Nevedomsky, V.V. Gusarov, Magnetic properties of synthetic $Ni_3Si_2O_5(OH)_4$ nanotubes, Europhys. Lett. 113 (4) (2016) 47006, http://dx.doi.org/10.1209/0295-5075/113/47006.

[43] J.D. Rall, M.S. Seehra, The nature of the magnetism in quasi-2D layered α-$Ni(OH)_2$, J. Phys.: Condens. Matter 24 (7) (2012) 076002, http://dx.doi.org/10.1088/0953-8984/24/7/076002.

[44] Z. Wang, M.S. Seehra, Magnetic investigations of phase transitions, exchange interactions, and magnetic ground state in nanosheets of β-$Co(OH)_2$, J. Phys.: Condens. Matter 29 (22) (2017) 225803, http://dx.doi.org/10.1088/1361-648X/aa6e77.

[45] R.L. Carlin, Magnetochemistry, Springer Science & Business Media, 2012.

[46] J.D. Rall, M.S. Seehra, E.S. Choi, Metamagnetism and nanosize effects in the magnetic properties of the quasi-two-dimensional system β-$Ni(OH)_2$, Phys. Rev. B 82 (18) (2010) 184403, http://dx.doi.org/10.1103/PhysRevB.82.184403.

[47] G.A. Bain, J.F. Berry, Diamagnetic corrections and Pascal's constants, J. Chem. Educ. 85 (4) (2008) 532, http://dx.doi.org/10.1021/ed085p532.

[48] S. Vonsovskii, Magnetism of Microparticles, Magnetizm Mikrochastits, Izdatel'stvo Nauka Glavnaya Redaktsiya Fiziko-Matematicheskoi Literatury, Moscow, 1973.

[49] W.J. Camp, J.P. Van Dyke, Isotropic magnets in two dimensions, J. Phys. C: Solid State Phys. 8 (3) (1975) 336, http://dx.doi.org/10.1088/0022-3719/8/3/012.

[50] L.J. de Jongh, Magnetic Properties of Layered Transition Metal Compounds, Vol. 9, Springer Science & Business Media, 1990.

[51] J. Nogués, J. Sort, V. Langlais, V. Skumryev, S. Suriñach, J.S. Muñoz, M.D. Baró, Exchange bias in nanostructures, Phys. Rep. 422 (3) (2005) 65–117, http://dx.doi.org/10.1016/j.physrep.2005.08.004.